PHYSICAL REVIEW B **80**, 075412 (2009)

Origin of the anomalous Slater-Pauling curve in cobalt-manganese alloy clusters

M. Pereiro,[1,*] D. Baldomir,[1] and J. E. Arias[2]

[1]*Departamento de Física Aplicada and Instituto de Investigacións Tecnolóxicas, Universidade de Santiago de Compostela, Santiago de Compostela E-15782, Spain*

[2]*Instituto de Investigacións Tecnolóxicas, Universidade de Santiago de Compostela, Santiago de Compostela E-15782, Spain*

(Received 26 February 2009; revised manuscript received 9 July 2009; published 10 August 2009)

Surprising enhancement of the magnetic moments recently observed in dilute Co-Mn alloy clusters is explained using *ab initio* electronic structure calculations. The calculated magnetic moments generally agree with the reported experimental data. An equation for calculating the magnetic moments of the Co-Mn alloy clusters has been derived to correct the deviations predicted by the rigid-band model and the virtual bound states approximation. A strategy is proposed to obtain the ground-state structures of the Co-Mn clusters and it was also put to the test of the experiment.

DOI: 10.1103/PhysRevB.80.075412 PACS number(s): 36.40.Cg, 31.15.A−, 75.20.Hr

I. INTRODUCTION

The exploration of bimetallic transition metal (TM) clusters is emerging as a promise field of research because of the opportunities they offer for developing magnetic recording devices and cluster-assembled materials with functions for medical applications.[1,2] Although the electronic and magnetic properties of bare TM clusters have been actively studied for several years, however less attention has been paid to their alloys because they represent both an experimental and theoretical challenge. Thus, for experimentalists is very difficult to control the stoichiometry of the alloy clusters using chemical methods, and for theoreticians, the determination of the ground-state geometries becomes a very difficult task, as commented later in the main text. The recent observation of the average magnetic moment enhancement in dilute Co-Mn alloy clusters[3] that contradicts the bulk behavior has presented an entirely unexpected dimension on the subfield of magnetic alloy clusters and it could pave the way for future possible applications such as, for example, in biomedicine as magnetic sensors. Although the search for the origin of the aforementioned observation has actively stimulated the research on Co-Mn alloy clusters,[3–6] however the answer still remains elusive. A possible explanation is based on the assumption that a virtual bound state (VBS) is formed below the highest occupied molecular orbital (HOMO) level and near the Mn site.[3] A VBS can be defined in the potential scattering model as a resonant scattering near impurity atoms in the host which induces a narrow peak in the conduction band density of states (DOS). Originally, the VBS model was developed by Friedel[7] to explain many of the physical properties of bulk magnetic alloys containing dilute magnetic species. It represents an improvement over the rigid-band (RB) model which is based on the assumption that the *s* and *d* bands are rigid in shape as atomic number of the alloy changes.[8] In this article, our calculations demonstrate that the origin of the anomalous behavior of the Slater-Pauling (SP) curve of Co-Mn alloy clusters does not require the formation of a VBS as suggested in Ref. 3, but is explained directly in terms of the magnetic moment provided by the Mn atoms and the "spin-flipping" of the electrons belonging to the Co-Mn bonding. Thus, with the aim of studying the magnetic properties of Co-Mn alloy clusters and elucidating the anomalous behavior of their SP curve, we have performed spin-unrestricted density-functional theory (DFT)-based calculations as implemented in the DEMON-KS3P5 program package.[9]

II. METHOD AND STRUCTURAL PROPERTIES

The electronic system consisting in Ω nuclei and η electrons is assumed to be described by the next Hamiltonian, which expressed in second quantization and in the Born-Oppenheimer nonrelativistic approximation reads as

$$\hat{H} = \sum_{ij}^{\eta} \sum_{\nu\mu} c_{\nu i}^{*} c_{\mu j} \left(\langle \nu | -\frac{1}{2}\Delta | \mu \rangle - \sum_{k}^{\Omega} Z_k \langle \nu \| \mu \rangle \right) \hat{a}_i^{\dagger} \hat{a}_j + \frac{1}{2}\sum_{ijkl}^{\eta} \sum_{\nu\mu\alpha\beta} c_{\nu i}^{*} c_{\mu j}^{*} c_{\alpha k} c_{\beta l} \langle \nu\mu \| \alpha\beta \rangle \hat{a}_i^{\dagger} \hat{a}_k^{\dagger} \hat{a}_l \hat{a}_j + \hat{V}_{xc}^{\mathrm{GGA}}(\rho^{\sigma}, \nabla\rho^{\sigma}) \qquad (1)$$

where the Kohn-Sham orbitals $(|i\rangle)$ were expanded into atomic orbitals $|i\rangle = \Sigma_{\mu} c_{\mu i} |\mu\rangle$ in the linear combination of GAUSSIAN type-orbitals ansatz. The orbital basis sets of contraction pattern (2111/211*/311+) and (2211/311/411) were used in conjunction with the corresponding (5,3,3;5,3,3) and (3,4;3,4) auxiliary basis sets for Co and Mn, respectively.[10] Likewise, *ad hoc* model core potentials with contraction pattern (4:7,4) and (5:7,4) have been used for describing the inner electrons of Co and Mn atoms, respectively.[11] The kinetic and nuclear attraction energy of the electrons in an environment of Z_k nuclear charges are described by the one-electron term. The $\|$ symbol represents the $1/|\mathbf{r}-\mathbf{k}|$ operator, where $\mathbf{r}$ and $\mathbf{k}$ are the electron and nuclear position vectors, respectively. The two-electron operator represents the Coulomb repulsion energy of the electrons. In this case, the symbol $\|$ represents the $1/|\mathbf{r}_1-\mathbf{r}_2|$ operator for the electrons with coordinates $\mathbf{r}_1$ and $\mathbf{r}_2$. The last term in Eq. (1) is the exchange-correlation energy and we have used here the form proposed in Ref. 12 which is a function of the spin-dependent electron density $(\rho^{\sigma}, \sigma = \uparrow, \downarrow)$ and its gradient in the generalized gradient approximation (GGA). We have

1098-0121/2009/80(7)/075412(8)

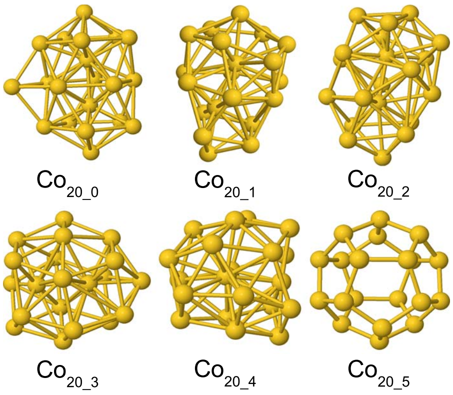

FIG. 1. (Color online) Illustration of the guessed structures of the Co$_{20}$ cluster. The structures are ordered from left to right and top to bottom by increased relative energy. The notation Co$_{20\_m}$ stands for the mth energetic isomer.

adopted the former GGA functional in our DFT calculations because it was reported in Ref. 11 that it represents a dramatical improvement in the calculated binding energies of Co clusters. The total energy of the system is calculated adding the nuclear repulsion energy $(\Sigma_{a>b}^{\Omega}(Z_a Z_b)/|\mathbf{r}_a - \mathbf{r}_b|)$ to the electronic contribution. A wide set of spin multiplicities ranging from 1 up to a maximum of 61, depending on the selected cluster, was checked to ensure that the lowest-energy electronic and magnetic configuration is reached. More information about the computational details can be found elsewhere.[13] Hereafter, all calculated results refer only to the Co-Mn alloy 20 atom clusters. We have also performed electronic structure calculations of some guessed geometries of the Co-Mn alloy clusters with $\Omega = 25$ and 30 in a range of Mn concentration less than 0.3, but the obtained results slightly differ from that of the $\Omega = 20$ case, i.e., we observed that the calculated magnetic moments of clusters with $\Omega = 25$ and 30 increase with the impurity concentration as $\Omega = 20$ clusters do. Accordingly, the conclusions drawn from the Co-Mn clusters with $\Omega = 20$ can be extended to clusters with greater size.

The search for the global minima of the Co-Mn alloys 20 atom clusters was planned as a multistage strategy combining an unbiased search method, i.e., a basin-hopping[14] algorithm, in conjuction with a molecular mechanics method.[15] In the reoptimization procedure of the clusters, we have made use of the Polak-Ribière algorithm[16] without any symmetry constraint and the root-mean-square gradient was set to 10^{-4} Kcal/(mol Å). In a first stage of the calculation method, the initial guessed structures of the Co$_{20}$ cluster were taken from three different sources, namely, the structures were provided by the *GMIN* code[14] which uses the basin-hoping algorithm, the existing databases,[17] and proposed by us. After that, they were reoptimized with the *HyperChem* code[15] with the intention to obtain the ideal candidate to the lowest-energy structure of the Co$_{20}$ cluster. The converged guessed structures are illustrated in Fig. 1 and the structural and energetic parameters are reported in Table I. The ground-state structure (Co$_{20\_0}$) is a capped double icosahedron. The cohesive energy and the number of nearest-neighbor Co-Co bonds reveal that the most stable structure is also the most compact one although the average first-neighbor distance is a little bit higher than the rest of structures plotted in Fig. 1. In a second stage, the rest of guessed structures of the Co$_m$Mn$_n$ alloy clusters were built from the geometry of the Co$_{20}$ cluster but this time $m-n$ Co atoms swap positions with n Mn atoms. The assumption is underpinned by three arguments: first, the ionic radii (r_a) of Co and Mn atoms are pretty close i. e., 1.25 Å and 1.26 Å, respectively.[19] Second, we have calculated the size of the Thomas-Fermi screening[7] outside the atomic sphere of the Mn atoms (Z_{Mn})

$$Z_{\mathrm{TF}} = Z_{\mathrm{Mn}}(1 + r_a\sqrt{4\pi\eta(\epsilon_{\mathrm{HOMO}})})e^{-r_a\sqrt{4\pi\eta(\epsilon_{\mathrm{HOMO}})}} \tag{2}$$

and it is vanishingly small because the DOS at the HOMO level $[\eta(\epsilon_{\mathrm{HOMO}})]$ provided by our DFT calculations are large [see Fig. 2(c)], so that the exponent in Eq. (2) is $r_a\sqrt{4\pi\langle\eta(\epsilon_{\mathrm{HOMO}})\rangle} \simeq 247.58$, where $\langle\eta(\epsilon_{\mathrm{HOMO}})\rangle$ represents the average over the lowest-energy Co-Mn alloy series clusters with $\Omega = 20$. Thus, the size effects are negligible and the addition of Mn atoms to the cluster should slightly distort their environment. Third, we have performed a geometry optimization of Co$_3$, Co$_2$Mn$_1$, Co$_4$, and Co$_3$Mn$_1$ clusters by means of spin-unrestricted DFT calculations[9] and the results show that the elongation of the Co-Mn average bond length with respect to the Co-Co one is less than 0.15 Å. In consequence, the substitution of cobalt atoms by Mn atoms should slightly distort the geometric structure of the clusters. This fact has also been observed in Ref. 3.

Another specific difficulty of alloy clusters is the great number of possibilities they offer to distribute the solute atoms over the sites at a given geometrical arrangement of the

TABLE I. Average first-neighbor distance (d$_{\text{Co-Co}}$), number of nearest-neighbor Co-Co bonds ($N_{\text{Co-Co}}$) per atom, relative (ΔE), and cohesive (E$_c$) energies of Co$_{20}$ cluster isomers. The geometry notation is that of Fig. 1. The point groups are determined from Ref. 18.

Cluster	Point group	d$_{\text{Co-Co}}$ (Å)	$N_{\text{Co-Co}}$/atom	ΔE (eV)	E$_c$ (eV)
Co$_{20\_0}$	C_{2v}	2.46	3.55	0.00	1.78
Co$_{20\_1}$	C_1	2.39	3.00	0.26	1.76
Co$_{20\_2}$	C_1	2.38	3.05	0.35	1.76
Co$_{20\_3}$	C_1	2.39	2.85	0.95	1.73
Co$_{20\_4}$	C_1	2.39	2.85	0.98	1.73
Co$_{20\_5}$	I_h	2.44	1.50	7.85	1.38

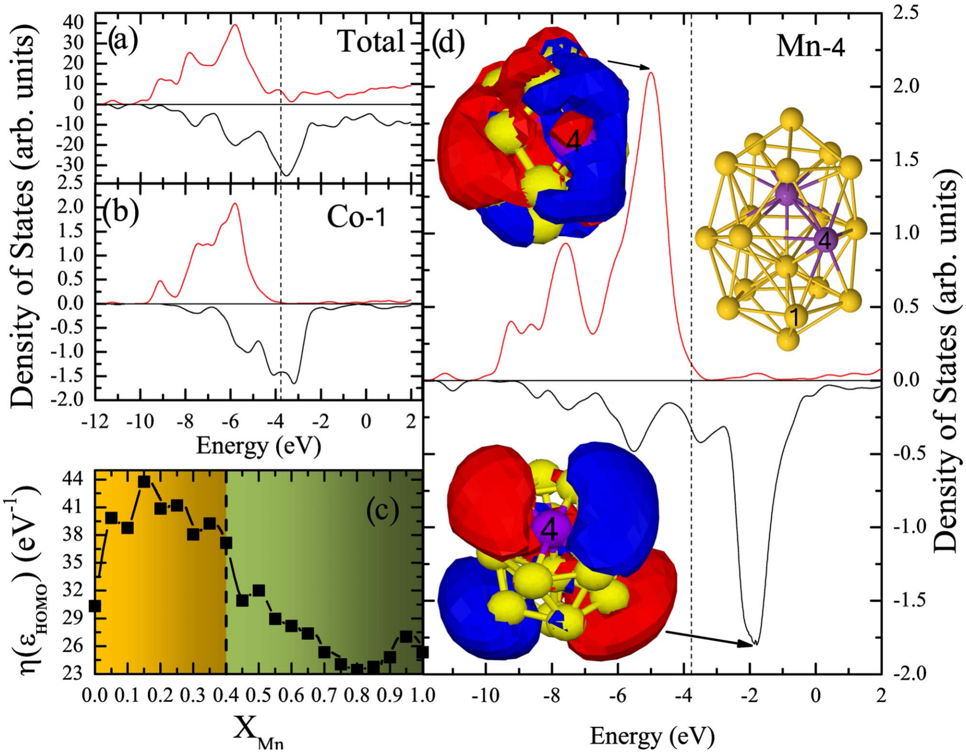

FIG. 2. (Color online) Plot of the spin-polarized DOS for (a) $Co_{18}Mn_2$, (b) Co-1, and (d) Mn-4, where the labels 1 and 4 represent the site number of Co and Mn atoms, respectively. In (b) and (d), we have only plotted the contribution of the *d* orbitals because *s* and *p* orbitals are of less importance. The upper-half part of the figures is for spin-up electrons while the lower half is for the spin-down electrons. The atoms of (b) and (d) are labeled in the geometric structure. We have also plotted the shape of the delocalized molecular orbitals for the higher-lying occupied and lower-lying unoccupied levels of $Co_{18}Mn_2$ cluster with the aim of showing the bonding and antibonding character of the orbitals, respectively. The dotted vertical lines represent the HOMO level. In (c), DOS at the HOMO level is plotted against the Mn concentration.

atoms. Thus, for example, in the case of $Co_{10}Mn_{10}$ the number of possible homotops for a geometry with inequivalent positions is $C_{10}^{20}=\frac{20!}{10!^2}\simeq 1.8\times 10^5$. With the aim of overcoming the aforementioned point, we have planned out a strategy consisting in optimize the geometries of the 20 homotops belonging to the $Co_{19}Mn_1$ cluster. As starting point, every structure was built from the optimized geometry of Co_{20} cluster but substituting a Co by a Mn atom at the 20 accessible positions of the cluster. After that, we performed a geometry optimization of the 20 homotops to obtain the stability of them as a function of the position occupied by the Mn atom. The rest of Co-Mn alloy clusters were created by replacing the cobalt atoms by Mn atoms at the positions with the lowest energy and once again they were reoptimized in geometry. We examined the method for the case of $Co_{18}Mn_2$ homotops where one of the two Mn atoms was attached to the position with the lowest energy and the other Mn was positioned in the rest of available sites. After the optimization procedure, we have observed that the lowest-energy structure was the one with Mn atoms in the lowest-energy positions and the energy of the other geometries was estimated to be 3.22 eV greater than the ground-state cluster. We have also put the geometry optimization method to the test of the experiment[20] as shown in Table II. The ionization potentials provided by our DFT calculations are in good agreement with the available experimental results and consequently, our reported structures should be very close to the ground-state structures of the Co-Mn alloy series clusters with $\Omega=20$. The lowest-energy structures are illustrated in Fig. 3 and the geometrical properties are collected in Table III. The Co-Mn alloy geometries converged in slightly distorted structures of that of the Co_{20}. In particular, the distance of the atom labeled as 12 in Fig. 3 to the rest of atoms belonging to the cluster is gradually reduced with the enhancement of the Mn concentration up to the $Co_{15}Mn_5$ cluster which elongates the distance. For the rest of clusters, the distance persists approximately unaltered. This point is reflected in the average nearest-neighbor distance for Co-Co bonding reported in Table III. It is also important to comment that the average nearest-neighbor distances for the Co-Co, Mn-Mn, and Co-Mn bondings are in general very close each other (see Table III). This results favor the assumption commented above that the addition of Mn atoms just only alters

TABLE II. Ionization potentials (in eV) for Co_mMn_n clusters with $\Omega=20$. The experimental data were taken from Ref. 20.

n	0	1	2	3	4	5
Theory	5.45	5.54	5.60	5.38	5.51	5.40
Experiment	5.45	5.44	5.37	5.34	5.31	5.23

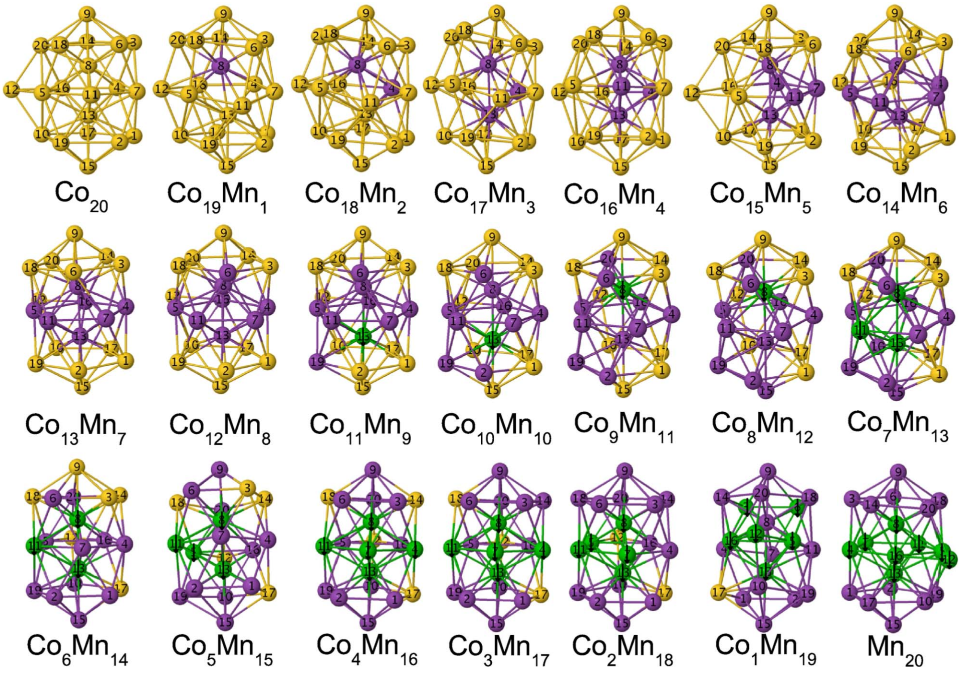

FIG. 3. (Color online) Illustration of the ground-state structures for Co-Mn binary clusters with $\Omega=20$. Co atoms are shown with yellow spheres whereas Mn atoms are represented with spheres in magenta. The green color (downwards arrow) represents the Mn atoms that couple antiferromagnetically with the rest of atoms of each cluster.

a little bit the geometry of the ground-state structure of Co_{20} cluster. To conclude the structural discussion, and with the aim to show how the Mn atoms diffuse into the Co ones, it is convenient to define an order parameter that is positive and close to 1 when the phase separation or segregation takes place and close to 0 when the mixing or disorder is the main contribution to the arrangement of the Mn atoms in the cluster. The parameter which meets the aforementioned conditions is the chemical order and it is thus defined as

$$\Gamma = \frac{N_{i-i} + N_{j-j} - N_{i-j}}{N_{i-i} + N_{j-j} + N_{i-j}} \tag{3}$$

where N_{i-j} represents the number of nearest-neighbor $i-j$ bonds (with i=Co and j=Mn). The values of Γ reported in Table III are plotted in Fig. 4. It is easily observed in Fig. 4 the asymmetry of the chemical order parameter with respect the dash vertical line. Thus, at low concentrations of Mn atoms Γ decreases more rapidly than for higher concentra-

TABLE III. Structural properties of the lowest-energy Co-Mn alloy clusters with $\Omega=20$. We report the average nearest-neighbor distance for the Co-Co, Mn-Mn, and Co-Mn bondings. The chemical order defined in Eq. (3) is also provided in the last column. The interatomic distances are given in Å.

Cluster	$d_{\text{Co-Co}}$	$d_{\text{Mn-Mn}}$	$d_{\text{Co-Mn}}$	Γ
Co_{20}	2.46			1.00
$Co_{19}Mn_1$	2.39		2.42	0.63
$Co_{18}Mn_2$	2.38	2.51	2.40	0.45
$Co_{17}Mn_3$	2.38	2.31	2.40	0.22
$Co_{16}Mn_4$	2.40	2.39	2.37	0.13
$Co_{15}Mn_5$	2.49	2.43	2.42	0.17
$Co_{14}Mn_6$	2.49	2.43	2.45	0.08
$Co_{13}Mn_7$	2.50	2.46	2.43	0.06
$Co_{12}Mn_8$	2.50	2.46	2.44	0.06
$Co_{11}Mn_9$	2.50	2.45	2.44	0.04
$Co_{10}Mn_{10}$	2.50	2.45	2.44	0.11
Co_9Mn_{11}	2.50	2.45	2.44	0.08
Co_8Mn_{12}	2.49	2.45	2.44	0.08
Co_7Mn_{13}	2.48	2.46	2.45	0.17
Co_6Mn_{14}	2.49	2.46	2.45	0.28
Co_5Mn_{15}	2.48	2.46	2.46	0.28
Co_4Mn_{16}		2.46	2.46	0.39
Co_3Mn_{17}		2.46	2.46	0.55
Co_2Mn_{18}		2.46	2.46	0.72
Co_1Mn_{19}		2.46	2.47	0.84
Mn_{20}		2.46		1.00

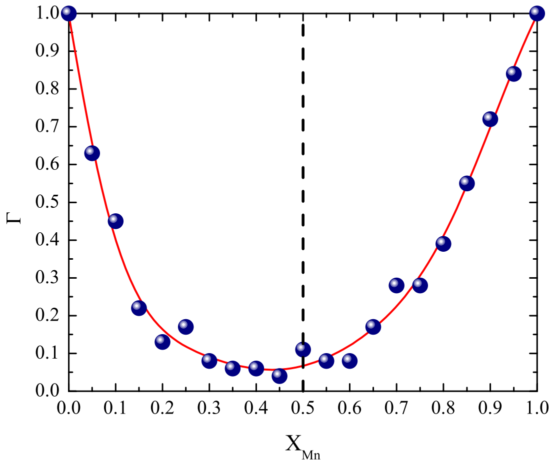

FIG. 4. (Color online) Chemical order parameter as a function of the Mn concentration. The solid line is a polynomial fitting to the numerical values of Γ and serves as a guide to the eye to appreciate the asymmetry of the chemical order parameter with respect to the dash vertical line (midpoint of the Mn concentration).

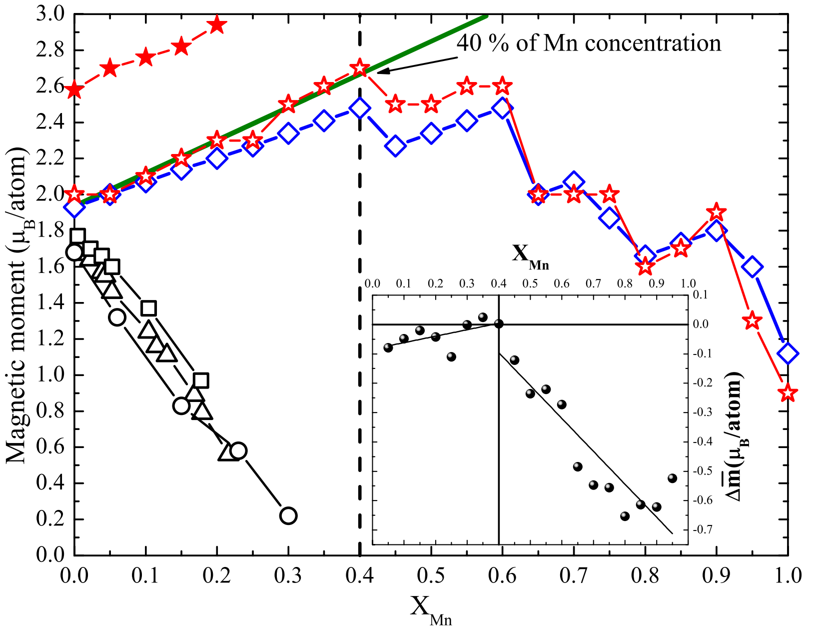

FIG. 5. (Color online) Magnetic moments per atom of Co_mMn_n clusters with $\Omega=20$ calculated in this work (empty star symbol) and measured in Ref. 3 (filled star symbol). The data for the Co-Mn bulk are taken from Ref. 21 (△ and □ symbols) and Ref. 22 (○ symbol). The solid line represents the linear fitting of the magnetic moments for the clusters with $n \leq 8$ and it retains a slope of 1.83 μ_B. The diamond points are the expecting magnetic moments according to Eq. (5). The inset represents the difference between the magnetic moments per atom of the Co first neighbors of Mn atoms ($\bar{m}_{\text{alloy}}$) in the Co_mMn_n and their Co counterparts ($\bar{m}_{Co_{20}}$) in Co_{20} cluster ($\Delta\bar{m}=\bar{m}_{\text{alloy}}-\bar{m}_{Co_{20}}$) as a function of Mn concentration. The linear fitting is a guide to the eye.

tions of them so that the mixing is favored in an interval of X_{Mn} ranging approximately from 0.15 to 0.65. The reason for that behavior is attributed to the positions occupied by the Mn atoms in the range of low concentration. As can be seen from Fig. 3, the impurity atoms swap positions with the inner Co atoms. The number of bondings between the inner positions and the rest of atoms is higher than the outer-shell positions. Thus, the number of Co-Mn bondings is favored for lower concentrations of the impurity and in consequence Γ decrease rapidly. But however, for higher concentrations of the Mn atoms, the process is not inverted and the cobalt atoms occupy mainly the outer-shell positions instead of the inner ones.

III. RESULTS AND DISCUSSION

The anomalous behavior of the SP curve in Co-Mn alloy clusters compared to the CoMn bulk[21,22] is shown in Fig. 5. The magnetic moments per atom (empty star symbol) increase with a slope of 1.83 μ_B up to a Mn concentration of 40%, after which the average magnetic moments tend to decrease with increasing Mn concentration. The above results are in very good agreement with the available experimental measurements (filled star symbol) reported in Ref. 3 (1.7 μ_B and 40%, respectively). The discrepancy with the numerical data (about 0.6 μ_B in average) may be related to the omission of the orbital moment contribution since the total magnetic moment is $\langle \vec{M} \rangle = 2\langle \vec{S} \rangle + \langle \vec{L} \rangle$. However, according to the results of the calculations performed for binary TM clusters reported in Ref. 4, the orbital moments represent a very small correction to the total magnetic moment and consequently underpins our approximation. Likewise, the source of error could also be ascribed to a wrong assignment of the ground-state structures of Co-Mn alloy cluster, but however it is unlikely because the measured value of the magnetic moment[23] in the case of the Co_{20} cluster is about 2.04 μ_B which is very close to our predicted value of 2.00 μ_B.

The negative slope ($\sim$6.0 μ_B per Mn substitution) of the SP curve for the bulk CoMn alloy, which is in contrast to the cluster behavior, is explained on the basis of the VBS concept,[7] i.e., a resonant scattering of the conduction electrons at the Mn sites which induces a narrow peak above the Fermi level for both spin channels. This point was confirmed by *ab initio* band structure calculations.[24] In the case of the CoMn alloy clusters, the first attempt to explain the positive slope was also based on the assumption of the existence of a VBS but this time only the majority-spin VBS was conjectured to remain below the HOMO level.[3] However, we can rule out the existence of the VBS and come to the same conclusion if we admit two hypothesis: first, the assumptions of the naive RB model are valid and second, the spin-up *d* band of the alloy is fully occupied.[25] See, as an example, Fig. 2(a) above. Thus, under these conditions the alloy moment per average atom is given by

$$\langle \mu_{\text{alloy}} \rangle = \langle \mu_{\text{host}} \rangle - c\Delta Z \mu_B \tag{4}$$

where c is the impurity concentration per atom and ΔZ is the atomic number difference of the impurity relative to the host. For Co host doped with Mn impurities, $\Delta Z=-2$ and the slope of the average alloy magnetic moment relative to the host is positive and proportional to 2 μ_B, which is relatively close to the experimental value (1.7 μ_B) and our reported result (1.83 μ_B). The VBS approximation can predict successfully the SP curve behavior in most of the TM solid alloys whereas its application to alloy clusters is less reliable because of the lack of a periodic crystalline lattice.[26] Moreover, the VBS and RB model fail to predict the behavior of the SP curve for Mn concentrations greater than 40% because they are only valid for small concentrations of impurities.

We have derived a formula for the average magnetic moment of CoMn alloys that corrects Eq. (4) and takes into

TABLE IV. Average magnetic moments (in μ_B/atom) and number of Mn atoms [g(n)] that couple antiferromagnetically with the rest of atoms belonging to each cluster of the $\mathrm{Co}_m\mathrm{Mn}_n$ series, and with n ranging from 9 up to 20. The notation $\mathrm{N}^{\uparrow}_{\text{Mn-Mn}}$ ($\mathrm{N}^{\downarrow}_{\text{Mn-Mn}}$) represents the average number of nearest-neighbor bonds between a FM (AF) Mn atom and the rest of Mn atoms.

n	9	10	11	12	13	14	15	16	17	18	19	20
$\mu^{\downarrow}_{\text{Mn}}$	−0.98	−1.11	−1.45	−1.50	−2.39	−2.49	−2.31	−2.73	−2.67	−2.27	−2.97	−2.95
g(n)	1	1	1	1	3	3	4	5	5	5	6	8
$\mathrm{N}^{\uparrow}_{\text{Mn-Mn}}$	4.6	4.9	4.4	5.1	4.9	5.3	5.1	5.3	5.7	5.9	6.8	6.2
$\mathrm{N}^{\downarrow}_{\text{Mn-Mn}}$	7.0	8.0	8.0	8.0	8.3	8.7	8.5	8.4	8.8	9.4	7.3	8.8

account the antiferromagnetic (AF) coupling between the impurities

$$\langle\mu_{\text{alloy}}\rangle = m\langle\mu_{\text{Co}}\rangle + (n - g(n))\langle\mu^{\uparrow}_{\text{Mn}}\rangle - g(n)\langle\mu^{\downarrow}_{\text{Mn}}\rangle \qquad (5)$$

where m and n are the number of Co and Mn atoms in the cluster, respectively, and $g(n)$ is the number of Mn atoms that couple antiferromagnetically with the rest of atoms[27] (see Table IV). In Fig. 3, we have also plotted in green (downwards arrow) the Mn atoms that couple antiferromagnetically to their neighbors. The averaged magnetic moments per atom and per clusters with different Mn compositions obtained from our DFT calculations for Co and Mn atoms are $\langle\mu_{\text{Co}}\rangle=1.93$, $\langle\mu^{\uparrow}_{\text{Mn}}\rangle=3.30$, and $\langle\mu^{\downarrow}_{\text{Mn}}\rangle=2.15$ μ_B/atom. The values (diamond points) provided by Eq. (5) are plotted in Fig. 5. To gain more insight into the physics behind Eq. (5) and based on the results provided by the electronic structure calculations, we have identified a double mechanism that explains the magnetic enhancement trend for Co-Mn clusters below 40% of Mn concentration and the successive fast dropping of the magnetic moment.

The first mechanism resides in the role played by the Mn atoms, as reflected in Eq. (5). First, the clusters increase their magnetic moments due to the addition of the Mn moments up to a maximum of 2.7 μ_B/atom and then they decrease their moments because of the AF alignment of some Mn atoms with the rest of atoms belonging to the cluster. We have plotted in Fig. 6 the magnetization density of $\mathrm{Co}_{12}\mathrm{Mn}_8$ and $\mathrm{Co}_{11}\mathrm{Mn}_9$ to see how the clusters evolve from a ferromagnetic (FM) configuration to an AF at a critical concentration of the impurity. The red surface surrounding the Mn atom indicates an AF coupling with the rest of atoms while the blue surface indicates a FM alignment. The onset of Mn atoms with negative magnetic moment resides mainly in a Mn-Mn charge transferring. The values of $\mathrm{N}^{\uparrow}_{\text{Mn-Mn}}$ and $\mathrm{N}^{\downarrow}_{\text{Mn-Mn}}$ reported in Table IV indicate that the AF Mn atoms are the ones which establish more bondings with the rest of Mn atoms in relation to the FM Mn atoms. To exemplify the explanation, we have plotted in Fig. 7 the spin-polarized DOS for the Mn-13 and Mn-16 atoms of the $\mathrm{Co}_{11}\mathrm{Mn}_9$ cluster. The Mn-13 atom is coupled antiferromagnetically to the rest of Mn and Co atoms (see Fig. 3). The elevated number of bondings make that the Mn-13 atom share more electrons with its Mn environment. This produces a charge transferring from the spin-up channel of the Mn-13 atom to the spin-up channel of the Mn atoms surrounding it, that is for example the case of Mn-16. Thus, at a critical number of the Mn-Mn bondings (close to 7) the Mn-13 atom becomes antiferromagnetic.

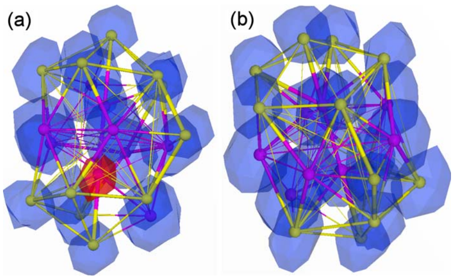

FIG. 6. (Color online) Isosurface plot of the magnetization density $(m(\mathbf{r})=[\rho^{\uparrow}(\mathbf{r})-\rho^{\downarrow}(\mathbf{r})]\mu_B)$ for (a) $\mathrm{Co}_{11}\mathrm{Mn}_9$ and (b) $\mathrm{Co}_{12}\mathrm{Mn}_8$. The Co and Mn atoms are illustrated by the yellow and magenta spheres, respectively. The blue surfaces represent a positive value for the magnetization density whereas the red surface indicates a negative value.

The second mechanism involves also the Co atoms and the "spin-flipping" of the electrons belonging to the Co-Mn bonding. Although the explanation have been exemplified to the $\mathrm{Co}_{18}\mathrm{Mn}_2$ cluster, it is applicable to the rest of calculated clusters with $1 \leq n \leq 8$. For these clusters, the DOS of Mn atoms shows a higher-lying occupied bonding orbital for spin-up electrons and a lower-lying (a few eV above HOMO level) empty antibonding orbital for spin-down electrons [see Fig. 2(d)], while for Co first-neighbor atoms the DOS manifests an increase in the spin-up population [see Fig. 2(b)]. In consequence, and based on the Mulliken population analysis, the electrons involved in the Co-Mn bonding move from the spin-down channel of Mn atoms to the spin-up channel of the Co first-neighbor atoms. This mechanism contributes to raise the magnetic moment of both Mn and Co neighbor atoms [see inset and text of the caption in Fig. 5]. However, the process stops at a critical concentration of the Mn atoms because the spin-up channel of the available Co atoms does not admit more electrons. Thus, in the range with n varying from 9 to 19, the process reverse and there is a charge transferring from the Mn spin-up channel to the Co neighbors spin-down one. In this case, the Mn and also the Co neighbor atoms [see inset in Fig. 5] decrease their moments.

It is also interesting finally to comment that the nonmonotonic decrease in the magnetic moments at the area above 40% of Mn concentration (see Fig. 5) is attributed to the discontinuity of g(n) with the concentration of the Mn impurity. Thus, for example, g(n) is equal to 1 in the range $9 \leq n \leq 12$. The average magnetic moments of the AF Mn atoms reported in Table IV are approximately constant in this

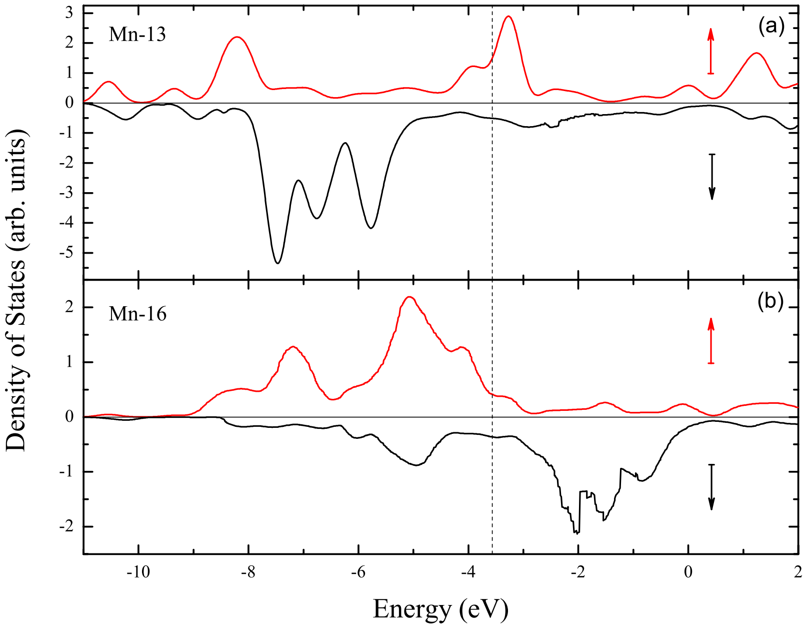

FIG. 7. (Color online) Plot of the spin-polarized DOS for (a) Mn-13 and (b) Mn-16 atom of $Co_{11}Mn_9$ cluster. The upper-half area of figure (a) and (b) is for spin-up electrons while the lower-half area is for spin-down electrons. The dotted vertical line represents the HOMO level.

range and consequently the total magnetic moment per atom of the clusters with $9 \leq n \leq 12$ is not reduced. The behavior changes drastically for n=13, where g(13)=3 and $\mu^{\downarrow}_{\text{Mn-13}} = -2.39\ \mu_B$/atom. The onset of the discontinuity in g(13) and the consequently enhancement of $\mu^{\downarrow}_{\text{Mn-13}}$ causes a reduction in the total magnetic moment of Co_7Mn_{13} cluster. The same kind of explanation still persists for the rest of clusters with higher Mn concentration.

IV. SUMMARY

In summary, the magnetic moment enhancement of CoMn clusters below 40% of Mn concentration and its successive fast dropping has been explained using first-principles electronic structure calculations. The explanation resides mainly on the magnetic role played by the Mn atoms and the “spin-flipping” of the electrons belonging to the Co-Mn bonding. Moreover, a formula [Eq. (5)] has also been proposed for calculating the magnetic moments of the Co-Mn alloy clusters. This equation represents an improvement over the results provided by both the RB model and the VBS approximation.

ACKNOWLEDGMENTS

The authors acknowledge the Centro de Supercomputación de Galicia for the computing facilities. M.P. acknowledges the Isabel Barreto program for financial support. The work also was supported by both the Ministerio de Educación y Ciencia and Xunta de Galicia under projects No. MAT2006-10027 and No. INCITE08PXIB236052PR, respectively.

---

*Corresponding author; manuel.pereiro.lopez@usc.es

[1] J. Bansmann *et al.*, Surf. Sci. Rep. **56**, 189 (2005).

[2] C. Binns *et al.*, J. Phys. D **38**, R357 (2005).

[3] S. Yin, R. Moro, X. Xu, and W. A. de Heer, Phys. Rev. Lett. **98**, 113401 (2007).

[4] G. Rollmann, S. Sahoo, A. Hucht, and P. Entel, Phys. Rev. B **78**, 134404 (2008).

[5] S. Ganguly, M. Kabir, S. Datta, B. Sanyal, and A. Mookerjee, Phys. Rev. B **78**, 014402 (2008).

[6] N. Shen, J. Wang, and L. Zhu, Chem. Phys. Lett. **467**, 114 (2008).

[7] J. Friedel, Nuovo Cim. **7**, (Suppl.), 287 (1958).

[8] J. C. Slater, J. Appl. Phys. **8**, 385 (1937); L. Pauling, Phys. Rev. **54**, 899 (1938).

[9] A. St-Amant and D. R. Salahub, Chem. Phys. Lett. **169**, 387 (1990)

[10] S. Huzinaga, J. Andzelm, M. Klobukowski, E. Radzio-Andzelm, Y. Sakai, and H. Tatewaki, *GAUSSIAN Basis Sets for Molecular Calculations* (Elsevier, Amsterdam, 1984).

[11] M. Pereiro, D. Baldomir, M. Iglesias, C. Rosales, and M. Castro, Int. J. Quantum Chem. **81**, 422 (2001).

[12] J. P. Perdew, J. A. Chevary, S. H. Vosko, K. A. Jackson, M. R. Pederson, D. J. Singh, and C. Fiolhais, Phys. Rev. B **46**, 6671 (1992); **48**, 4978 (1993).

[13] M. Pereiro, D. Baldomir, and J. E. Arias, Phys. Rev. A **75**, 063204 (2007).

[14] D. J. Wales and J. P. K. Doye, J. Phys. Chem. A **101**, 5111 (1997).

[15] HyperChem(TM) Professional 7.51, Hypercube, Inc., 1115 NW 4th Street, Gainesville, Florida 32601, USA.

[16] R. Fletcher, *Practical Methods of Optimization* (John Wiley & Sons, Chichester, 1996), Chap. 4, p. 83.

[17] D. J. Wales, J. P. K. Doye, A. Dullweber, M. P. Hodges, F. Y. Naumkin, F. Calvo, J. Hernández-Rojas, and T. F. Middleton, The Cambridge Cluster Database, URL: http://www-wales.ch.cam.ac.uk/CCD.html.

[18] http://www.colby.edu/chemistry/PChem/scripts/ABC.html.

[19] C. Kittel, *Introduction to Solid State Physics* (John Wiley & Sons, Hoboken, 2005), p. 71.

[20] G. M. Koretsky, K. P. Kerns, G. C. Nieman, M. B. Knickelbein, and S. J. Riley, J. Phys. Chem. A **103**, 1997 (1999).

[21] J. Crangle, Philos. Mag. **2**, 659 (1957).

[22] R. Poerschke, *Magnetic Properties of Metals: d-Elements, Alloys and Compounds* (Springer-Verlag, Berlin, 1991), Chap. 2, p. 52.

[23] M. B. Knickelbein, J. Chem. Phys. **125**, 044308 (2006).

[24] V. S. Stepanyuk, R. Zeller, P. H. Dederichs, and I. Mertig, Phys. Rev. B **49**, 5157 (1994).

[25] R. C. O'Handley, *Modern Magnetic Materials: Principles and Applications* (John Wiley & Sons, New York, 2000), Chap. 5, p. 153.

[26] J. Friedel, Adv. Phys. **3**, 446 (1954).

[27] The numerical values of $g(n)$ provided by our DFT calculations are

$$g(n) = \begin{cases} \theta(n-8.5) & 1 \le n \le 12 \\ \theta(n-14.5)+3 & 13 \le n \le 15 \\ 5 - \dfrac{(n-23)}{24} \prod_{i=16}^{18} (n-i) & 16 \le n \le 20 \end{cases},$$

where $\theta(n)$ is the Heaviside theta function.